Journal of Materials Chemistry A

Cobalt and nitrogen-codoped ordered mesoporous carbon as highly efficient bifunctional catalysts for oxygen reduction and hydrogen evolution reactions

Journal:	*Journal of Materials Chemistry A*
Manuscript ID	TA-ART-07-2018-006864.R2
Article Type:	Paper
Date Submitted by the Author:	01-Aug-2018
Complete List of Authors:	Liu, Xiaojun; American University, Chemistry; Oakland University, Chemistry Li, Wenyue; American University, Chemistry Zou, Shouzhong; American University, Chemistry

Journal of Materials Chemistry A

ARTICLE

Cobalt and nitrogen-codoped ordered mesoporous carbon as highly efficient bifunctional catalysts for oxygen reduction and hydrogen evolution reactions

Received 00th July 2018,
Accepted 00th January 20xx

DOI: 10.1039/x0xx00000x

www.rsc.org/

Xiaojun Liu,[a,b] Wenyue Li[a] and Shouzhong Zou[a]*

The high cost and limited reserves of noble metals such as Pt have hampered their large-scale commercial applications in oxygen reduction reaction (ORR) and hydrogen evolution reaction (HER). Herein, we developed a simple silica template approach to form porous carbons codoped with nitrogen and cobalt as highly efficient bifunctional electrocatalysts for ORR and HER. The resulted porous carbons exhibited excellent electrocatalytic activity for ORR in alkaline media, which compares favorably with that of commercial Pt/C (20 wt%), and had superior durability and excellent methanol tolerance. The porous carbons also showed superior performance for HER, with a low onset potential of -0.04 V, a Tafel slope of 49 mV dec^{-1}, an overpotential of -0.106 V at a current density of 10 mA cm^{-2}, and remarkable durability. These results demonstrate that the Co, N-doped carbons are promising bifunctional catalysts for fuel cell applications.

Introduction

The sustainability and environment concerns over the use of fossil fuels have prompted intense research on alternative energy conversion and storage systems. Oxygen reduction reaction (ORR) and hydrogen evolution reaction (HER) are key processes in various energy technologies.[1] Development of efficient and economical catalysts for both ORR and HER is of critical importance in these technologies. Noble metal catalysts (e.g. Pt, Pd) have been commonly used in ORR and HER due to their high catalytic activities for these processes. However, the high cost and scarcity of these precious metals severely limit their large-scale commercial applications. Therefore, considerable efforts have been devoted to developing efficient and low-cost electrocatalysts to partially or even completely replace precious metal-based catalysts. A wide range of active and low-cost non-noble metal catalysts, including first row transition metal (Fe, Co)/nitrogen-codoped carbon,[2-7] and metal-free heteroatom (N, B, P, S) doped carbon[8-11] have been actively explored. Among them, nitrogen/cobalt-doped carbon materials are one of the most promising candidates due to their low cost, excellent electrocatalytic activity, long durability and environmental friendliness.[4, 12] Despite the great progress achieved in the synthesis of carbon materials doped with heteroatoms, it remains a challenge to design and synthesize porous carbon with high surface area, hierarchical pores, homogeneous distribution of heteroatoms and high exposure of active sites. Moreover, previously reported carbon-based electrocatalysts exhibited excellent catalytic activity for either ORR or HER,[13-26] but dual activity for both ORR and HER has not been extensively reported.[11, 27-31] In the few reported work, the ORR and HER activities often come from different components in the composite catalysts.[27-31] In some cases, metal or metal phosphide nanoparticles were embedded in the carbon materials to enhance their catalytic activities through either effecting their electronic properties such as electron transfer rate and work function,[28] or serving as active sites for the second reaction.[27, 29, 30] Potential compromises from the presence of nanoparticles are the decrease of effective surface area and the blockage of the active sites.[32] A primary motivation of the present study is to explore the possibility of using metal and nitrogen codoped carbon as a single component catalyst for both HER and ORR. We would like to point out that the term "bifunctional" here is different from that used in overall water electrolysis where it refers to activity for both HER and oxygen evolution reaction (OER), or in regenerative fuel cell and metal air battery literature where it refers to activity for both ORR and OER.[33-37]

Herein, we developed cobalt and nitrogen codoped ordered mesoporous carbons as a highly active and durable bifunctional catalyst for ORR and HER. The use of melamine and poly-phenylenediamine as precursors yielded high nitrogen content in the catalysts, and the silica colloid template produced uniform mesopores facilitating reactant access to active sites. The obtained catalysts possess a high specific surface area (413.1 m^2 g^{-1}) and uniform pore size (ca. 22 nm) and exhibit excellent electrocatalytic performance for both ORR and HER. To the best of our knowledge,

[a] Department of Chemistry, American University, Washington, DC 20016, USA.
[b] Present address: Department of Chemistry, Oakland University, Rochester, MI 48309, USA
*Email - szou@american.edu

†Electronic Supplementary Information (ESI) available: Additional experimental data and discussion, Table S1-S6 and FigureS1-S7. See DOI: 10.1039/x0xx00000x

the present catalyst is among the most efficient non-precious metal/nitrogen-codoped carbon bifunctional catalysts reported for ORR and HER, with performances comparable to the state-of-the-art commercial Pt/C.

Experimental Section

Chemicals. Melamine (99%), o-phenylenediamine (oPD), ammonium peroxydisulfate (APS, 98%), $CoCl_2$•$6H_2O$ (⩾98%), $HClO_4$ (70%), HF (⩾48%), H_2SO_4 (95-98%), KOH (≥85%), colloidal silica (LUDOX TM-40, ca. 22 nm in dia., 40 wt% in water), and Nafion solution (5 wt%) were purchased from Sigma Aldrich and used without further purification. Commercial 20 wt% Pt/C catalysts were purchased from Fuel Cell store. Water (18.2 MΩ•cm) was supplied from a Milli-Q water purification system.

Material synthesis. The preparation procedure of Co and N codoped ordered mesoporous carbon is summarized in **Scheme 1**. In a typical preparation, 3 g of oPD, 6 g of melamine, 1.5 g of $CoCl_2$•$6H_2O$ and 22.5 g of colloidal silica were dissolved/dispersed in 200 mL of 1 M HCl at ambient conditions under vigorous stirring for 10 minutes to form a uniform mixture. Then 100 mL of 1 M HCl containing 3 g APS was added to the above mixture under vigorous stirring to initiate the polymerization of oPD. The mixture was stirred for 24 h in an ice water bath (<5 ^oC) and then dried by rotary evaporation. The resultant dark green composites were ground into powder and pyrolyzed under an argon gas flow at an elevated temperature between 700 and 1000 ^oC for 1 h with a temperature ramp rate of 5 $^oC\ min^{-1}$. Afterwards, the silica colloids were removed by using a 24% HF solution. Subsequently, the sample was subject to a heat treatment again in an argon atmosphere for 1 h at the same temperature. Finally, the obtained sample was soaked in 0.5 M H_2SO_4 at 90 ^oC for 6 h to remove cobalt particles. The resultant samples were denoted as Co,N-CT, where T (=700, 800, 900, or 1000 °C) represents the pyrolysis temperature.

Characterization. The morphology of the obtained materials was examined by a high-resolution transmission electron microscope (HRTEM, JEOL JEM-2100). X-ray diffraction (XRD) patterns were recorded at room temperature using a Bruker D8 diffractometer with Cu Kα radiation (λ = 0.1541 nm). Raman spectra were collected using a confocal LabRAM HR800 spectrometer (Horiba JobinYvon, FR.) and an excitation wavelength of 514 nm from an argon ion laser. The nitrogen adsorption/desorption isotherms were recorded at 77 K using a Micromeritics ASAP 2020 Plus instrument. X-ray photoelectron spectroscopy (XPS) measurements were conducted on a PHI X-tool spectrometer with Al Kα radiation.

Electrochemistry.

(1) **ORR**, all electrochemical measurements were carried out in a three-electrode glass cell with a CHI 630A electrochemical workstation (CH Instruments). A platinum wire and a Ag/AgCl electrode (1M KCl) were used as the counter and reference electrode, respectively. The working electrode was a rotating ring-disk electrode (RRDE) consisted of a glassy carbon disk (GCE, 5.0 mm in diameter) surrounded by a Pt ring (Pine Instrument). Prior to surface coating, the working electrode was polished sequentially with aqueous slurries of 1, 0.3, and 0.05 μm alumina powders on a polishing micro-cloth. A typical catalyst ink was prepared by dispersing 4 mg of the sample in 1 mL of a 4:1 (v/v) ethanol/water mixture along with 40 μL of the Nafion solution under sonication. 15 μL of the obtained catalyst ink was pipetted onto the mirror-like GCE surface and dried at room temperature for 20 min with a catalyst loading of 0.24 mg cm^{-2}. Before starting a test, the electrolyte (0.1 M KOH) was purged with N_2 or O_2 for at least 30 min to saturate the electrolyte. For all of the experiments, the electrodes were cycled 50 times at 50 mV s^{-1} to obtain a reproducible cyclic voltammogram before RRDE experiments. The RRDE tests were measured from 0.2 to – 1.0 V (vs Ag/AgCl) in an O_2-saturated electrolyte at different rotating speeds with a potential sweep rate of 10 mV s^{-1}. The Ag/AgCl (1 M KCl) electrode was calibrated with respect to a reversible hydrogen electrode (RHE), in 0.1 M KOH and all of the reported potentials were converted to RHE scale using the equation: E(RHE) = E (Ag/AgCl) + 0.970 V.

(2) **HER**, electrochemical measurements were performed in a three-electrode cell with a CHI 630A electrochemical workstation using a GCE (diameter 3.0 mm) with various catalysts as the working electrode, a Ag/AgCl electrode as the reference electrode and a graphite rod as the counter electrode. 0.5 M H_2SO_4 was used as the electrolyte. 4 mg of the respective catalyst powders was dispersed in 1 mL of 1:1 (v/v) water/ethanol mixture and 40 μL Nafion solution to form the catalyst ink. The mixture was sonicated for 30 min. 5 μL suspension was pipetted onto the GCE and fully dried at room temperature. The catalyst was cycled 200 times to obtain a stable CV before other tests. Linear sweep voltammetry was carried out from 0 to −0.8 V (vs Ag/AgCl) at 5 mV s^{-1}. The electrochemical impedance spectroscopy (EIS) was carried out in the frequency range of 10^{-2} to 10^5 Hz with an AC voltage amplitude of 5 mV in 0.5 M H_2SO_4. The Ag/AgCl (1 M KCl) electrode was calibrated with respect to a reversible hydrogen electrode (RHE) in 0.5 M H_2SO_4 and the reported potentials were converted to the RHE scale using the equation: E(RHE) = E (Ag/AgCl) + 0.227 V.

Results and discussion

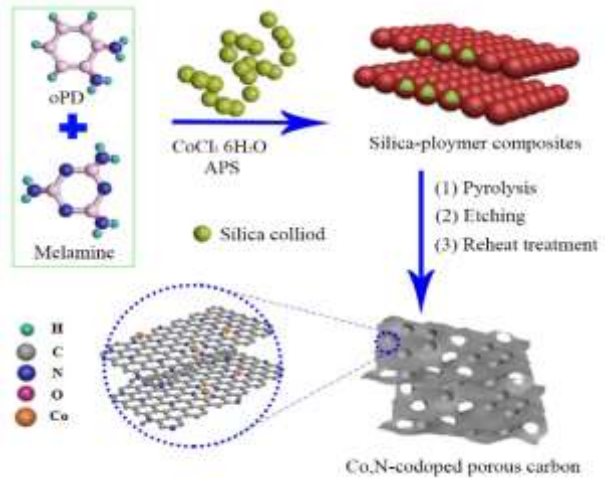

Scheme 1. Schematics of the procedures for the preparation of the mesoporous carbon codoped with Co and N.

A schematic diagram of the synthetic procedures is shown in scheme 1. The Co,N-CT (T=700, 800, 900, 1000 °C) carbon materials were fabricated by employing o-phenylenediamine (oPD) and melamine as the sources for both carbon and nitrogen, and silica particles as a template. The procedure typically involves the following four steps: (a) polymerization of oPD on the silica template surface initiated by ammonium peroxydisulfate (APS), and the entrapment of Co ions and melamine in the polymer to form silica-polymer composites, which may facilitate the uniform distribution of Co and N in the obtained catalysts. (b) carbonization of the polymer layer by pyrolysis at elevated temperatures; (c) removal of the silica template by HF etching to obtain mesoporous carbon-based materials; (d) further pyrolysis at the same temperature, followed by H_2SO_4 leaching to remove unstable metallic cobalt nanoparticles.

The structure and morphology of the as-prepared samples were first characterized by TEM. The Co,N−C900 are made of graphene-like carbon sheets (**Figure 1a**), which contain a number of uniform pore structures resulted from the sacrificial silica colloid templates. The magnified image of Co,N−C900 further demonstrates the presence of the pore structures (**Figure 1b**). The high-resolution TEM image (**Figure. 1c**) shows that the Co,N-C900 possess small partially crystalline domains with a lattice spacing of about 0.375 nm, suggesting the formation of graphite structure.[38] Energy-dispersive X-ray spectroscopic (EDX) elemental mapping was performed to identify the distribution of elements in the Co,N-C900 sample. Co and N-containing species were uniformly distributed throughout the porous carbon structure (**Figure 1d**). The close resemblance of the Co and N distributions suggests the possible formation of Co−N moieties, which have been proposed to be the highly active sites for ORR and HER. The corresponding EDS spectrum of Co,N-C900 confirms the presence of Co and N with carbon (**Figure S1**). TEM images of Co,N-CT prepared at different pyrolysis temperatures are similar to that of Co,N-C900 as shown in **Figure S1**.

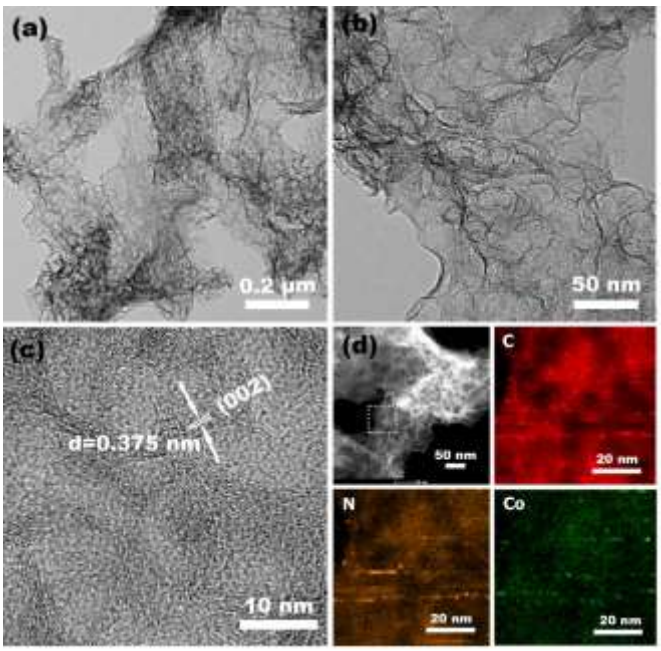

Figure 1. (a, b, c) TEM images of the as-obtained Co,N-C900 and (d) the corresponding elemental mapping showing the distribution of C (red), N (orange) and Co (green).

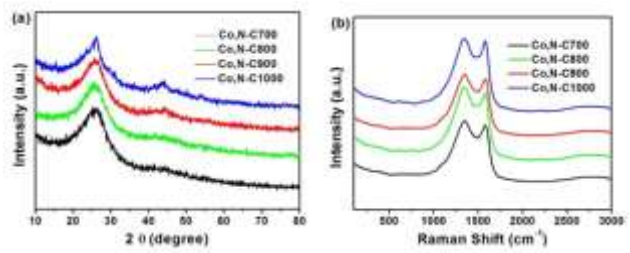

Figure 2 (a) XRD patterns and (b) Raman spectra of Co,N-CT samples.

Figure 2a shows XRD diffraction patterns for the as-prepared samples. All Co,N-CT samples showed two broad peaks located at 24.7° and 43.4°, which can be assigned to the (002) and (101) diffraction of the graphitic carbon, respectively.[39] No other detectable peaks appeared in the XRD pattern, implying that the acid leaching process removed most of the cobalt particles and the cobalt atoms might be incorporated into the carbon framework in disordered forms. This result is in good agreement with the TEM observations in **Figure 1**. The Raman spectra of Co,N-CT samples are displayed in **Figure. 2b**. All of the samples showed a similar pattern with a D band at 1353 cm^{-1} (related to the defects) and a G band at 1584 cm^{-1} (related to the crystalline graphite).[40] The peak intensity ratio of the D to G band (I_D/I_G) gradually decreased with increasing pyrolysis temperature: 1.08 (Co,N-C700) > 1.05 (Co,N-C800) > 1.03 (Co,N-C900) > 1.01 (Co,N-C1000), indicating the degree of graphitization improved with the increasing temperature.[41, 42]

ORR Performance

To assess the ORR catalytic activity, cyclic voltammetry (CV) was first conducted on the four samples in 0.1 M KOH saturated with N_2 and O_2 respectively as shown in **Figure 3a**. The current density was obtained by normalizing the recorded current to the geometric area of the supporting glassy carbon electrode. In the O_2-saturated 0.1 M KOH solution, all four samples exhibited distinct cathodic reduction peaks with the peak potential at +0.75 V for Co,N-C700, +0.85 V for Co,N-C800, +0.88 V for Co,N-C900 and +0.86 V for Co,N-C1000, whereas only a featureless quasi-rectangular voltammogram was obtained in the N_2 saturated electrolyte. These results suggest that the reduction peaks are from O_2 reduction and all of the samples are active for ORR. To further characterize the ORR activity of these samples, linear sweep voltammograms (LSV) of all samples were collected by using a rotating ring disk electrode (RRDE) and benchmarked with a commercial Pt/C (20wt%). Consistent with the CV results, among all of the samples, Co,N-C900 exhibited the highest ORR activity, as evident by its highest onset (+0.97 V) and half wave (+0.85 V) potentials and limiting current density at +0.4 V (5.82 mA cm^{-2}), which are comparable to Pt/C (+0.97 V, +0.88 V, and 5.68 mA cm^{-2}, respectively) **(Figure 3b and Table S1)**.

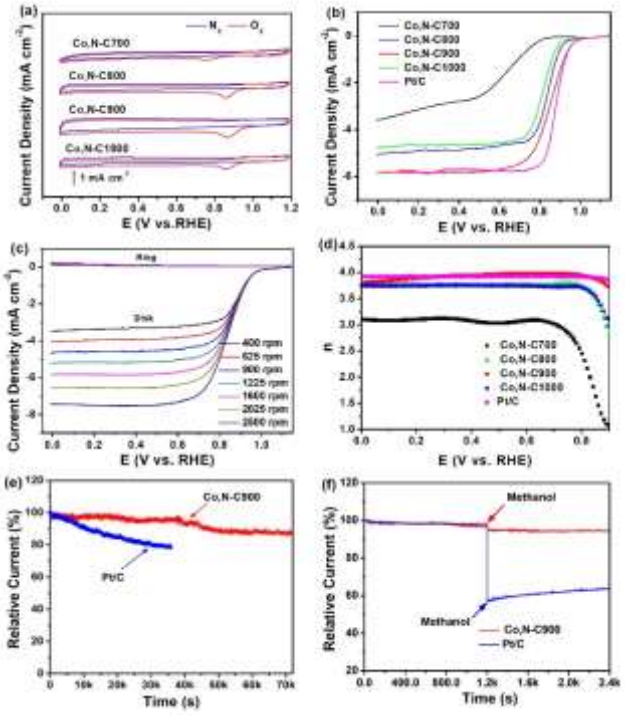

Figure 3. (a) Cyclic voltammograms of Co,N-CTs in N_2 and O_2 -saturated 0.1 M KOH; scan rate 10 mV s^{-1}. (b) Linear sweep voltammograms of Co,N-CTs and Pt/C at the electrode rotation rate of 1600 rpm and potential scan rate of 10 mV s^{-1}; (c) RRDE polarization curves for Co,N-C900 in O_2-saturated 0.1 M KOH, with the ring potential set at +1.49 V; (d) Variation of the number of electron transfer (n) with the electrode potential; (e) Chronoamperometric profiles of Co,N-C900 and Pt/C in O_2-saturated 0.1 M KOH at +0.88 V at a rotation speed of 900 rpm. (f) same as (e) but with the addition of 3 M methanol at 1200 s as indicated by the arrows.

To gain insights into the ORR kinetics, RRDE measurements were performed at various rotation rates. A typical set of RRDE voltammograms from Co,N-C900 is shown in **Figure 3c**. The current density increased with the increasing electrode rotating speed (from 400 to 2500 rpm) and the corresponding ring currents were at least an order of magnitude lower, which signifies that the formation of peroxide species is insignificant. The number of electron transfer (n) at different potentials can be calculated from the RRDE measurements using the following equation:

$$n = \frac{4I_D}{I_D + I_R / N} \qquad (1)$$

where I_D represents the disk current, I_R is the ring current, and N is the RRDE collection efficiency (20%). The n value calculated from the RRDE data from Co,N-C900 is 3.71-3.99 from 0 to +0.9 V, suggesting the ORR proceeds largely as a 4e reaction which is similar to Pt/C (**Figure 3d**). In contrast, significantly lower electron transfer numbers were obtained from other samples in the same potential range (**Table S1**).

In addition to the excellent ORR activity, Co,N-C900 also exhibited excellent stability and methanol tolerance. The chronoamperometric responses of Co,N-C900 and Pt/C (20 wt%) were recorded at the peak potential in O_2-saturated 0.1 M KOH with an electrode rotation speed of 900 rpm. **Figure 3e** showed that the ORR activity of Co,N-C900 catalyst decreased only 11.5% after 20 h, while a 22% loss after only 10 h was observed on Pt/C catalyst, indicating much superior ORR activity stability of Co,N-C900 over Pt/C. The methanol tolerance of Co,N-C900 and Pt/C was tested in 0.1 M KOH with the addition of 3 M methanol at 1200s. As illustrated in **Figure 3f**, the current density of Pt/C suffered from a marked drop of about 40%, indicating surface poisoning from methanol oxidation on the catalyst. In contrast, the Co,N-C900 displayed almost invariant current density. These results demonstrated that Co,N-C900 is far less sensitive to methanol crossover than Pt/C catalyst. The ORR performance of Co,N-C900 is substantially better than other recently reported Co,N-doped carbon materials, especially after the catalyst surface area (the BET specific area times the catalyst loading in each study) is taken into account (**Table S2)**. In addition, it is worth noting that the Co,N-C900 catalyst also exhibited ORR activity in acidic media with an $E_{1/2}$ of ca. 0.75 V, which is comparable to Co,N-doped carbon catalysts developed by others (**see Figure. S2**).

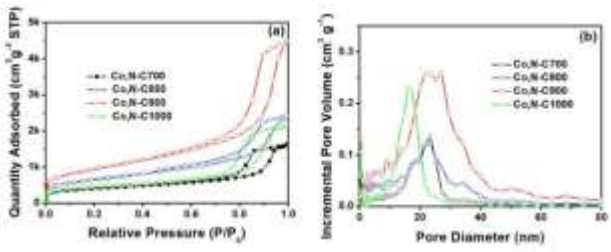

Figure 4. (a) Nitrogen adsorption–desorption isotherms and (b) pore size distribution of Co,N-CTs.

To unveil key factors contributing to the remarkable ORR performance of Co,N-C900, the porosity and specific surface area of the catalysts were measured by means of the nitrogen sorption technique. The N_2 adsorption and desorption isotherms are shown in **Figure 4a**. The hysteresis loop in the high relative pressure range (P/P_0>0.8) on the isotherms for all samples is a characteristic of type IV adsorption with a large specific surface area and mesoporous structure.[43, 44] Consistent results were obtained in the pore size distribution (PSD) analysis where the PSD was calculated from the desorption curve by density functional theory (DFT). From **Figure 4b**, it can be seen that Co,N-C700, Co,N-C800 and Co,N-C900 exhibited a narrow PSD which is centered around 22 nm, very close to the diameter of the colloidal silica templates (ca. 22 nm). This result is consistent with TEM observations. In contrast, Co,N-C1000 showed a strong peak at around 16 nm, suggesting that higher pyrolysis temperature results in the collapse of the pores. The specific surface area obtained from the Brunauer-Emmett-Teller (BET) measurements increased gradually with the increasing pyrolysis temperature from 173.8 $m^2 g^{-1}$ (Co,N-C700), to 326.6 $m^2 g^{-1}$ (Co,N-C800) and 413.1 $m^2 g^{-1}$ (Co,N-C900). However, the surface area of the Co,N-C1000 is dramatically lower at 274.5 $m^2 g^{-1}$, again due to the collapse of pores during the pyrolysis process. **Table S3** summarized the BET surface area and the total pore volume. The highest specific surface area of Co,N-C900 provides more active sites for ORR and the uniform mesoporous pores facilitate the mass transport of reactants to the active sites. These factors together contribute to the highest ORR activity observed on Co,N-C900. To support this assertion, control experiments were carried out on Co,N-C900 prepared without adding the silica template (denoted as Co,N-NTC900). As expected the specific surface area and the pore volume of Co,N-NTC900 dropped significantly (**Table S4**), so did the ORR performance. The half wave potential moved to +0.79 V and the limiting current density decreased to 2.7 mA cm^{-2} (**Figure S3**) signifying insufficient accessible active sites.

Another critical factor governing the ORR activity is the chemical nature of the active sites. X-ray photoelectron spectroscopy (XPS) analysis revealed the presence of C1s, N1s, O1s and Co2p in Co,N-CTs (**Figure 5** and **Figure S4**). Based on the integrated peak area, the atomic concentrations of these elements were estimated and summarized in **Table S5**. It can be seen that the nitrogen content decreased substantially from 10.9% for Co,N-C700 to 8.62% for Co,N-C800, 6.37% for Co,N-C900 and 4.26% for Co,N-C1000 , while the Co content increased slightly (**Figure 5a**). The deconvolution of the high resolution N 1s spectra (**Figure 5b** and F**igure S4**) yielded five peaks at 398.3, 398.5, 400.1, 401.0 and 402.3 eV which revealed the presence of pyridinic, Co-bonded, pyrrolic, graphitic and oxidized pyridinic N.[45-47] These results suggest that N atoms successfully embedded into the carbon matrix, and some of them are associated with Co species to form the Co-N sites (Co-N_x), which play an important role in ORR and HER.[4, 48, 49] Moreover, as displayed in the Co 2p XPS spectra (**Figure 5c**), three peaks located at 780.3, 781.5 and 783.0 eV can be assigned to the Co-C-N, Co-N and Co(II) species, respectively.[50-52] The absence of a peak at ca. 778 eV indicates the absence of metallic Co, corroborating with the absence of Co nanoparticles in the TEM images. Of particular interest in **Figure 5d** is that Co,N-C900 exhibited the highest content of graphitic N and Co-N_x, which have been proposed as the most likely active sites for ORR,[53] and also likely major contributors to the highest ORR performance observed on Co,N-C900. To examine the role of cobalt species, catalysts without Co (denoted as N-C900) was prepared under the same conditions as Co,N-C900. The specific surface area and the pore volume of N-C900 are slightly smaller than Co,N-C900, but the ORR activity of N-C900 is significantly inferior to Co,N-C900 (**Figure. S3**), indicating the important role played by the Co species, most likely Co-N_x species.

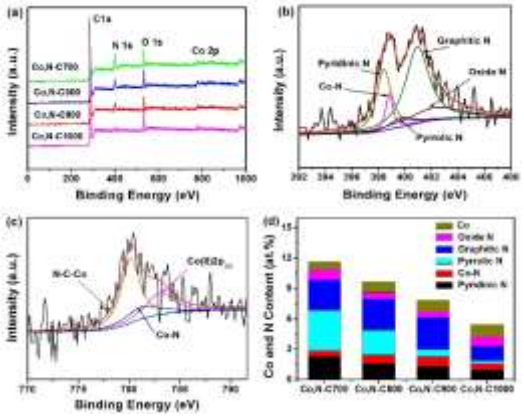

Figure 5. (a) XPS survey spectra from Co,N-CTs. (b, c) high-resolution scans of N1s (b) and Co 2P (c) of Co, N-C900; (d) Percent contents of N and Co.

HER Performance

To demonstrate the bifunctional catalytic activities, the electrocatalytic HER activities of Co,N-CT samples were investigated in 0.5 M H_2SO_4 solution by LSV using the commercial Pt/C (20 wt%) as a benchmark (**Figure 6a)**. All samples exhibited nonzero cathodic currents at sufficiently negative electrode potentials. Among all of the Co,N-CT samples, Co,N-C900 showed the best performance with a onset potential of -0.04 V and an overpotential (η) of -0.106 V at the current density (j) of 10 mA cm^{-2}, which is close to -0.004 V and -0.04 V for Pt/C. **Figure 6b** displays the Tafel plots of the polarization curves. Pt/C exhibited a Tafel slope of 30 mV dec^{-1}, which is consistent with the known mechanism of HER on Pt.[54-56] The Co,N-C700, Co,N-C800, Co,N-C900 and Co,N-C1000 showed a Tafel slope of 114 mV dec^{-1}, 77 mV dec^{-1}, 49 mV dec^{-1} and 79 mV dec^{-1}, respectively. A lower Tafel slope corresponds to more favourable HER kinetics. Tafel slope values have been frequently used as HER mechanistic diagnostic criteria for various catalysts.[56-58] It is generally accepted that there are three major reaction steps for HER in acidic electrolytes, including a primary proton discharge step (Volmer reaction, with a Tafel slope of 118 mV dec^{-1}) followed either by an electrochemical desorption step (Heyrovsky reaction, with a Tafel slope of 42 mV dec^{-1}) or a recombination step of adsorbed hydrogen atoms on catalyst surfaces (Tafel reaction, with a Tafel slope of 29 mV dec^{-1}).[56] The Co,N-C900 exhibited the lowest Tafel slope of 49 mV dec^{-1} among the Co,N-CT samples, which suggests that HER at Co,N-

C900 likely proceeded via the Volmer–Heyrovsky mechanism, and that the electrochemical desorption step is rate limiting.[56] The HER performance of Co,N-900 is better than most of recently reported non-noble metal-based HER catalysts (**Table S6)**. Co,N-C900 also showed HER activity in 0.1 M KOH solution, but the performance is inferior to the acidic media (**Figure S5**), which have been reported by others on various catalysts.[10, 17, 59, 60]

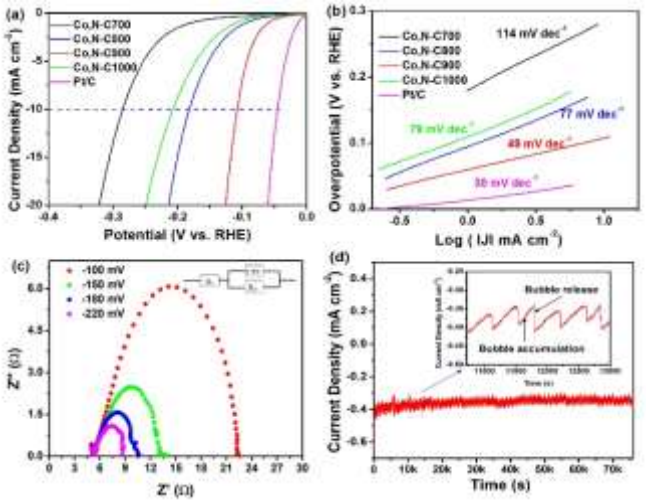

Figure 6 (a) LSVs of Co,N-CTs and Pt/C for HER in 0.5 M H_2SO_4. Potential sweep rate: 5 mV s^{-1}. (b) The corresponding Tafel curves derived from (a). (c) Electrochemical impedance spectra and the equivalent circuit of Co,N-C900 at various potentials for HER in 0.5 M H_2SO_4. (d) Time dependence of the HER current density of Co,N-C900 at -0.04 V. Inset: the impacts of H_2 bubbles on the HER current.

Electrochemical impedance spectroscopy (EIS) measurement was carried out to further probe the electron transfer kinetics involved. **Figure 6c** depicts the Nyquist plots of the Co,N-C900 at various potentials. The impedance data were fitted to an equivalent circuit depicted in the inset of **Figure 6c**, where R_{ct} is the charge transfer resistance, R_s represents the uncompensated solution resistance, and CPE is the constant-phase element.[61, 62] The charge transfer resistance diminished markedly with decreasing applied potential, from 22.4 Ω at -100 mV to 8.9 Ω at -220 mV and the solution resistance was 5.8 Ω. Note that these R_{ct} are drastically lower than those of other HER catalysts at similar overpotentails, such as WS_2 nanoribbons (38 Ω at -250 mV),[63] MoS_2 on mesoporous graphene (1810 Ω at -90 mV),[64] N,S self-doped porous carbon nanosheets (72.4 Ω at -150 mV),[65] and hair-derived N,S self-doped porous carbon (32.1 Ω at -220 mV).[66] For comparison, the electrochemical impedance spectra at -0.20 V of various samples for HER are shown in **Figure S6**. Consistent with the HER activity, the R_{ct} is the smallest for Co,N-C900. A current–time plot was recorded at -0.04 V to probe the stability of the HER activity of Co,N-C900 (**Figure 6f**). The current remained nearly constant over a 20 h of continuous operation. The noise was a result of the alternate accumulation and release of hydrogen bubbles on the surface of the catalysts.

Control experiments were conducted to dissect factors contributing to the remarkable HER activity of Co,N-C900. The HER activity for catalysts prepared under the same protocol but without Co (denoted N-C900) is much lower than Co,N-C900 (**Figure S7**), suggesting the Co atoms enhance the HER activity. This observation corroborates with literature reports that Co-N_x species play an important role in HER.[4, 17] In addition, the HER performance of catalysts prepared without using the silica template (Co,N-NTC900) is significantly inferior to the Co,N-C900 and N-C900 (**Figure S7**). For example, at -0.12 V, the HER current density on Co,N-C900 is at least 50 times higher than on Co,N-NTC900. This notion suggests the presence of mesoporous structures is critical for enhancing the HER activity, probably through facilitating the access of reactants to active sites and creating extra active sites.

BET surface area has been extensively used as a criterion for high performing catalysts. To verify that the BET surface area is representative of the electrochemically active surface area, we measured the electrochemical double-layer capacitance (C_{dl}), which can be estimated by CV **(Figure S8)**. The Co,N-C900 exhibited a rectangle-like cyclic voltammogram between 0 and +0.1 V, which was maintained when the scan rate was increased from 40 mV s^{-1} to 240 mV s^{-1}. This observation suggests facile ion transport and good ionic conductivity, which agrees with the electrochemical impedance results (**Figure 7c**). The C_{dl} can be estimated from the slope of the linear fit of the average current density ($\Delta J = (J_a - J_c)/2$) at 0.05 V versus the potential scan rate plot.[67] The double layer capacitance of Co,N-C900 modified electrode measured by this method is 11.5 mF cm_{geo}^{-2} (normalized to GCE geometric area) which is higher than Co,N-C700 (5.4 mF cm_{geo}^{-2}), Co,N-C800 (9.4 mF cm_{geo}^{-2}) and Co,N-C1000 (8.1 mF cm_{geo}^{-2}). This result implies Co,N-C900 possess higher electrochemically active surface area, which is consistent with the BET surface area measurements. When the C_{dl} is normalized to the BET areas, the values for all catalysts converge to 10 μF cm_{BET}^{-2}, suggesting the BET assessed area is proportion to the electrochemically active area. Given that the BET surface area difference is less than three times among all of the Co,N-CT samples, other factors contribute more to the markedly higher HER activity for Co,N-C900. For example, at -0.12 V HER current density for Co,N-C900 is 19.1 mA cm_{geo}^{-2}, which is nearly 60 times of that for Co,N-C700 at 0.32 mA cm_{geo}^{-2}, and significantly larger than the BET surface area difference (**Table S3**). The similar adsorption-desorption isotherms in **Figure 4** suggest that the Co,N-CT have a similar type of the pores. A survey of different nitrogen species reveals that the Co,N-C900 has about 50% and 88% more Co-N and graphitic N, respectively, and 8 times less pyrrolic N than Co,N-C700 (**Table S5**). None of these factors individually could account for the observed HER activity difference. Other factors such as the synergistic effects of different N species, the location of various active sites, and the difference in the microstructure may need to be considered. Model catalysts with a more controlled structure are needed to pinpoint factors governing the high catalytic activity of the higher performing Co,N–doped carbon catalysts.

Conclusions

In summary, cobalt and nitrogen codoped carbons with high surface area and uniform pore structures have been successfully synthesized through a simple low-cost silica colloid template approach. The Co,N-C900 exhibited remarkable bifunctional electrocatalytic activities for oxygen reduction reaction and hydrogen evolution reaction with good stability. It is worth noting that the HER activity of the Co,N-900 surpasses most of the non-noble metal-based HER elctrocatalysts reported to date while its ORR activity is comparable to the commercial Pt/C (20wt%), but is more stable and insensitive to the presence of methanol. The enhanced ORR and HER activities were attributed to the synergistic effects from the presence of mesoporous structures, the high surface area, and the high percentages of graphitic N and Co-N_x species. This work demonstrates the feasibility of using single component Co and N codoped carbons as bifunctional catalysts for HER and ORR, departing from the composite materials where each component is responsible for catalysing one of the reactions. The developed catalyst may have potential applications in water electrolysis, fuel cells, and other energy storage and conversion applications.

Acknowledgements

This work was partially supported by the National Science Foundation (CHE-1559670) and American University.

Notes and references

1. C. Hu and L. Dai, *Angewandte Chemie International Edition*, 2016, **55**, 11736-11758.
2. M. Jahan, Q. Bao and K. P. Loh, *Journal of the American Chemical Society*, 2012, **134**, 6707-6713.
3. W. Niu, L. Li, X. Liu, N. Wang, J. Liu, W. Zhou, Z. Tang and S. Chen, *J. Am. Chem. Soc*, 2015, **137**, 5555-5562.
4. H.-W. Liang, S. Brüller, R. Dong, J. Zhang, X. Feng and K. Müllen, *Nat. Commun.*, 2015, **6**, 7992.
5. H.-W. Liang, W. Wei, Z.-S. Wu, X. Feng and K. Müllen, *Journal of the American Chemical Society*, 2013, **135**, 16002-16005.
6. Y. Hou, Z. Wen, S. Cui, S. Ci, S. Mao and J. Chen, *Advanced Functional Materials*, 2015, **25**, 872-882.
7. X. Liu, S. Zou and S. Chen, *Nanoscale*, 2016, **8**, 19249-19255.
8. K. Gong, F. Du, Z. Xia, M. Durstock and L. Dai, *Science*, 2009, **323**, 760-764.
9. L. Yang, S. Jiang, Y. Zhao, L. Zhu, S. Chen, X. Wang, Q. Wu, J. Ma, Y. Ma and Z. Hu, *Angewandte Chemie*, 2011, **123**, 7270-7273.
10. Y. Zheng, Y. Jiao, Y. H. Zhu, L. H. Li, Y. Han, Y. Chen, A. J. Du, M. Jaroniec and S. Z. Qiao, *Nat. Commun.*, 2014, **5**, 3783.
11. J. T. Zhang, L. T. Qu, G. Q. Shi, J. Y. Liu, J. F. Chen and L. M. Dai, *Angew. Chem.-Int. Edit.*, 2016, **55**, 2230-2234.
12. Y. Hou, Z. Wen, S. Cui, S. Ci, S. Mao and J. Chen, *Advanced Functional Materials*, 2015, **25**, 872-882.
13. B. Y. Guan, L. Yu and X. W. Lou, *Journal of the American Chemical Society*, 2016, **138**, 11306-11311.
14. H. Hu, L. Han, M. Yu, Z. Wang and X. W. Lou, *Energy Environ. Sci.*, 2016, **9**, 107-111.
15. S. Gadipelli, T. Zhao, S. A. Shevlin and Z. Guo, *Energy Environ. Sci.*, 2016, **9**, 1661-1667.
16. Y. Z. Chen, C. Wang, Z. Y. Wu, Y. Xiong, Q. Xu, S. H. Yu and H. L. Jiang, *Adv. Mater.*, 2015, **27**, 5010-5016.
17. X. Zou, X. Huang, A. Goswami, R. Silva, B. R. Sathe, E. Mikmeková and T. Asefa, *Angewandte Chemie*, 2014, **126**, 4461-4465.
18. H. Tang, H. Yin, J. Wang, N. Yang, D. Wang and Z. Tang, *Angewandte Chemie*, 2013, **125**, 5695-5699.
19. R. Silva, D. Voiry, M. Chhowalla and T. Asefa, *Journal of the American Chemical Society*, 2013, **135**, 7823-7826.
20. G. Wu, K. L. More, C. M. Johnston and P. Zelenay, *Science*, 2011, **332**, 443-447.
21. Y. Zhao, F. Zhao, X. Wang, C. Xu, Z. Zhang, G. Shi and L. Qu, *Angewandte Chemie International Edition*, 2014, **53**, 13934-13939.
22. C. H. Choi, S. H. Park and S. I. Woo, *ACS Nano*, 2012, **6**, 7084-7091.
23. B. Y. Guan, L. Yu and X. W. D. Lou, *Advanced Science*, 2017, **4**.
24. M. Sun, H. Liu, Y. Liu, J. Qu and J. Li, *Nanoscale*, 2015, **7**, 1250-1269.
25. M. Sun, D. Davenport, H. Liu, J. Qu, M. Elimelech and J. Li, *J. Mater. Chem. A*, 2018.
26. C. Wu, Y. Zhang, D. Dong, H. Xie and J. Li, *Nanoscale*, 2017, **9**, 12432-12440.
27. M. Kuang, Q. H. Wang, P. Han and G. F. Zheng, *Adv. Energy Mater.*, 2017, **7**.
28. J. Lu, W. J. Zhou, L. K. Wang, J. Jia, Y. T. Ke, L. J. Yang, K. Zhou, X. J. Liu, Z. H. Tang, L. G. Li and S. W. Chen, *ACS Catal.*, 2016, **6**, 1045-1053.
29. R. Wang, X. Y. Dong, J. Du, J. Y. Zhao and S. Q. Zang, *Adv. Mater.*, 2018, **30**.
30. L. Yang, Y. L. Lv and D. P. Cao, *J. Mater. Chem. A*, 2018, **6**, 3926-3932.
31. X. J. Zeng, J. L. Shui, X. F. Liu, Q. T. Liu, Y. C. Li, J. X. Shang, L. R. Zheng and R. H. Yu, *Adv. Energy Mater.*, 2018, **8**.
32. H. G. Zhang, H. Osgood, X. H. Xie, Y. Y. Shao and G. Wu, *Nano Energy*, 2017, **31**, 331-350.
33. Y. Yan, B. Y. Xia, B. Zhao and X. Wang, *J. Mater. Chem. A*, 2016, **4**, 17587-17603.
34. Z. F. Huang, J. Wang, Y. C. Peng, C. Y. Jung, A. Fisher and X. Wang, *Adv. Energy Mater.*, 2017, **7**.
35. C. Guan, H. J. Wu, W. N. Ren, C. H. Yang, X. M. Liu, X. F. Ouyang, Z. Y. Song, Y. Z. Zhang, S. J. Pennycook, C. W. Cheng and J. Wang, *J. Mater. Chem. A*, 2018, **6**, 9009-9018.
36. S. Zhao, L. T. Yan, H. M. Luo, W. Mustain and H. Xu, *Nano Energy*, 2018, **47**, 172-198.
37. J. Zhang, Z. Zhao, Z. Xia and L. Dai, *Nat Nanotechnol*, 2015, **10**, 444-452.
38. T. Kun, F. Lijun, W. R. J., Y. Linghui, T. Maria -

Magdalena, A. Markus and M. Joachim, *Adv. Energy Mater.*, 2012, **2**, 873-877.
39. R. Liu, D. Wu, X. Feng and K. Müllen, *Angewandte Chemie*, 2010, **122**, 2619-2623.
40. M. Sevilla and A. B. Fuertes, *ACS Nano*, 2014, **8**, 5069-5078.
41. L. Bing, D. Fang, X. Qiangfeng, Y. Li, S. Jingmei, Z. Cunman and C. Mei, *Adv. Energy Mater.*, 2016, **6**, 1600802.
42. L. Li, P. Dai, X. Gu, Y. Wang, L. Yan and X. Zhao, *J. Mater. Chem. A*, 2017, **5**, 789-795.
43. W. Qian, F. Sun, Y. Xu, L. Qiu, C. Liu, S. Wang and F. Yan, *Energy & Environmental Science*, 2014, **7**, 379-386.
44. X. Liu, Y. Zhou, W. Zhou, L. Li, S. Huang and S. Chen, *Nanoscale*, 2015, **7**, 6136-6142.
45. Z.-S. Wu, L. Chen, J. Liu, K. Parvez, H. Liang, J. Shu, H. Sachdev, R. Graf, X. Feng and K. Müllen, *Advanced Materials*, 2014, **26**, 1450-1455.
46. S. Gao, K. Geng, H. Liu, X. Wei, M. Zhang, P. Wang and J. Wang, *Energy Environ. Sci.*, 2015, **8**, 221-229.
47. T. Xing, Y. Zheng, L. H. Li, B. C. C. Cowie, D. Gunzelmann, S. Z. Qiao, S. Huang and Y. Chen, *ACS Nano*, 2014, **8**, 6856-6862.
48. Q. Li, R. Cao, J. Cho and G. Wu, *Advanced Energy Materials*, 2014, **4**, n/a-n/a.
49. L. Lai, J. R. Potts, D. Zhan, L. Wang, C. K. Poh, C. Tang, H. Gong, Z. Shen, J. Lin and R. S. Ruoff, *Energy & Environmental Science*, 2012, **5**, 7936-7942.
50. M. Li, X. Bo, Y. Zhang, C. Han, A. Nsabimana and L. Guo, *Journal of Materials Chemistry A*, 2014, **2**, 11672-11682.
51. R. L. Arechederra, K. Artyushkova, P. Atanassov and S. D. Minteer, *ACS Appl. Mater. Interfaces*, 2010, **2**, 3295-3302.
52. A. Morozan, P. Jegou, B. Jousselme and S. Palacin, *Physical Chemistry Chemical Physics*, 2011, **13**, 21600-21607.
53. Y.-Z. Chen, C. Wang, Z.-Y. Wu, Y. Xiong, Q. Xu, S.-H. Yu and H.-L. Jiang, *Advanced Materials*, 2015, **27**, 5010-5016.
54. P. Xiao, M. A. Sk, L. Thia, X. Ge, R. J. Lim, J.-Y. Wang, K. H. Lim and X. Wang, *Energy Environ. Sci.*, 2014, **7**, 2624-2629.
55. C. G. Morales-Guio, L.-A. Stern and X. Hu, *Chemical Society Reviews*, 2014, **43**, 6555-6569.
56. B. E. Conway and B. V. Tilak, *Electrochimica Acta*, 2002, **47**, 3571-3594.
57. D. A. Harrington and B. E. Conway, *Electrochimica Acta*, 1987, **32**, 1703-1712.
58. J. Xie, J. Zhang, S. Li, F. Grote, X. Zhang, H. Zhang, R. Wang, Y. Lei, B. Pan and Y. Xie, *Journal of the American Chemical Society*, 2013, **135**, 17881-17888.
59. A. B. Laursen, K. R. Patraju, M. J. Whitaker, M. Retuerto, T. Sarkar, N. Yao, K. V. Ramanujachary, M. Greenblatt and G. C. Dismukes, *Energy Environ. Sci.*, 2015, **8**, 1027-1034.
60. H. B. Zhang, Z. J. Ma, J. J. Duan, H. M. Liu, G. G. Liu, T. Wang, K. Chang, M. Li, L. Shi, X. G. Meng, K. C. Wu and J. H. Ye, *ACS Nano*, 2016, **10**, 684-694.
61. L. Liao, S. Wang, J. Xiao, X. Bian, Y. Zhang, M. D. Scanlon, X. Hu, Y. Tang, B. Liu and H. H. Girault, *Energy & Environmental Science*, 2014, **7**, 387-392.
62. Y. Ito, W. Cong, T. Fujita, Z. Tang and M. Chen, *Angewandte Chemie International Edition*, 2015, **54**, 2131-2136.
63. M. A. Lukowski, A. S. Daniel, C. R. English, F. Meng, A. Forticaux, R. J. Hamers and S. Jin, *Energy & Environmental Science*, 2014, **7**, 2608-2613.
64. L. Liao, J. Zhu, X. Bian, L. Zhu, M. D. Scanlon, H. H. Girault and B. Liu, *Advanced Functional Materials*, 2013, **23**, 5326-5333.
65. Y. Zhou, Y. Leng, W. Zhou, J. Huang, M. Zhao, J. Zhan, C. Feng, Z. Tang, S. Chen and H. Liu, *Nano Energy*, 2015, **16**, 357-366.
66. X. Liu, W. Zhou, L. Yang, L. Li, Z. Zhang, Y. Ke and S. Chen, *J. Mater. Chem. A*, 2015, **3**, 8840-8846.
67. H. Wang, Z. Lu, D. Kong, J. Sun, T. M. Hymel and Y. Cui, *ACS Nano*, 2014, **8**, 4940-4947.

TOC Graph

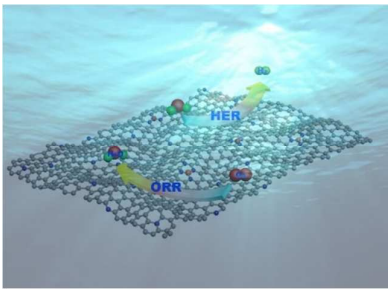

Co, N-codoped ordered mesoporous carbons showed excellent electrocatalytic activities for ORR and HER.